

Cite as: S. S. Shin *et al.*, *Science* 10.1126/science.aam6620 (2017).

# Colloidally prepared La-doped BaSnO<sub>3</sub> electrodes for efficient, photostable perovskite solar cells

Seong Sik Shin,<sup>1,2</sup> Eun Joo Yeom,<sup>1</sup> Woon Seok Yang,<sup>3</sup> Seyoon Hur,<sup>4</sup> Min Gyu Kim,<sup>5</sup> Jino Im,<sup>1</sup> Jangwon Seo,<sup>1</sup> Jun Hong Noh,<sup>1,6\*</sup> Sang Il Seok<sup>1,3\*</sup>

<sup>1</sup>Division of Advanced Materials, Korea Research Institute of Chemical Technology, 141 Gajeong-Ro, Yuseong-Gu, Daejeon 34114, Republic of Korea. <sup>2</sup>Massachusetts Institute of Technology, 77 Massachusetts Avenue, Cambridge, MA 02139, USA. <sup>3</sup>Perovaltronics Research Center, School of Energy and Chemical Engineering, Ulsan National Institute of Science and Technology, 50 UNIST-gil, Eonyang-eup, Ulju-gun, Ulsan 44919, Republic of Korea. <sup>4</sup>Department of Materials Science and Engineering, Seoul National University, Seoul, 151-744, Republic of Korea. <sup>5</sup>Beamline Research Division, Pohang Accelerator Laboratory (PAL), Pohang 790-784, Republic of Korea. <sup>6</sup>School of Civil, Environmental and Architectural Engineering, Korea University, Seoul 136-713, Republic of Korea.

\*Corresponding author. E-mail: seoksi@unist.ac.kr (S.I.S.); jhnoh@kriit.re.kr (J.H.N.)

Perovskite solar cells (PSCs) exceeding a power conversion efficiency (PCE) of 20% have mainly been demonstrated by using mesoporous titanium dioxide (mp-TiO<sub>2</sub>) as an electron-transporting layer. However, TiO<sub>2</sub> can reduce the stability of PSCs under illumination (including ultraviolet light). Lanthanum (La)-doped BaSnO<sub>3</sub> (LBSO) perovskite would be an ideal replacement given its electron mobility and electronic structure, but LBSO cannot be synthesized as well-dispersible fine particles or crystallized below 500°C. We report a superoxide colloidal solution route for preparing an LBSO electrode under very mild conditions (below 300°C). The PSCs fabricated with LBSO and methylammonium lead iodide (MAPbI<sub>3</sub>) show a steady-state power conversion efficiency of 21.2%, versus 19.7% for a mp-TiO<sub>2</sub> device. The LBSO-based PSCs could retain 93% of its initial performance after 1000 hours of full Sun illumination.

Fully solidified perovskite solar cells (PSCs) emerged (1, 2) after the use of methylammonium lead halide ( $\text{CH}_3\text{NH}_3\text{PbX}_3$ ; X is I and Br) perovskites as dyes in dye-sensitized liquid electrolyte solar cells by Miyasaka in 2009 (3). Since then, the power conversion efficiency (PCE) of these photovoltaic (PV) devices has increased at an incredible rate (4, 5). The common device architecture for PSCs includes a mesoporous (mp) oxide layer on top of a thin oxide blocking layer as an n-type electron-transporting layer (ETL) and an organic hole-transporting layer (HTL) such as 2,2',7,7'-tetrakis(*N,N*-di-p-methoxyphenyl-amine)9,9'-spirobifluorene (spiro-OMeTAD) and poly-triarylamine (PTAA) (6, 7). An inverted configuration has been reported by combining poly(3,4-ethylenedioxythiophene) polystyrene sulfonate (PEDOT:PSS) as an HTL and [6,6]-phenyl-C61 butyric acid methyl ester (PCBM) as an ETL (8). Generally, efficient PSCs are fabricated by using a mp-oxide ETL/perovskite/organic HTL configuration. In PSCs, TiO<sub>2</sub> is typically used as the mp-oxide; highly efficient PSCs (those exceeding a PCE of 20%) are fabricated with TiO<sub>2</sub> as the ETL, although the use of other oxide materials, such as SnO<sub>2</sub>, ZnO, and Zn<sub>2</sub>SnO<sub>4</sub>, has been reported (9–12).

Recently, the stability of PSCs upon exposure to moisture, heat, and light has attracted interest because PSCs must be able to withstand these conditions for their commercialization. The stability of PSCs can be determined by

several factors, including the instability of the perovskite material itself and the charge transport material, such as ETL and HTL, as well as the interface in the device configuration (4, 13–17). In particular, when mp-TiO<sub>2</sub> is used as an ETL, it negatively affects the device stability under ultraviolet (UV) illumination (14, 15, 18). Various strategies have been considered to improve the stability of PSCs, such as the replacement of TiO<sub>2</sub> (15), insertion of interfacial layers between the ETL and perovskite layers (14, 19), use of a UV filter or doping of TiO<sub>2</sub> to reduce UV-induced photocatalysis (15, 20), and introduction of a down-converting layer (18). However, an approach that does not require additional processes is to search for a new type of ETL to replace mp-TiO<sub>2</sub> and fabricate stable PSCs without damaging their performance.

BaSnO<sub>3</sub> (BSO) is an n-type semiconducting perovskite oxide with a wide band gap of 3.2 eV. It is used in various applications, e.g., as a transparent conducting oxide (TCO) (21), thin-film transistor (22), or gas sensor (23). In particular, La-doped BSO (LBSO) exhibits an unusually high electrical mobility of 320 cm<sup>2</sup> V<sup>−1</sup> s<sup>−1</sup> at room temperature (24) and has an inferior UV photocatalytic ability because of its small dipole moment, ascribed to the cubic perovskite structure without octahedra tilting (25, 26). However, LBSO films cannot be applied onto flexible or even glass substrates because of the high crystallization temperature of the LBSO perovskite phase of >1000°C (27). An approach for obtaining

a compact, crystalline LBSO thin film below at least 500°C is to coat a desired LBSO colloidal solution that includes well-dispersed precrystalline LBSO perovskite nanoparticles (NPs) onto the substrate. Introducing amorphous precursors containing peroxy groups could reduce the crystalline temperature to 900°C; the amorphous precursors are prepared by mixing aqueous barium chloride and tin chloride solutions with a solution of hydrogen peroxide and NH<sub>3</sub> in water (28, 29). However, the temperature is still too high to fabricate optoelectric devices on a glass substrate. Recently, Huang *et al.* reported a peroxy-precursor synthesis method for mp-BSO at 300°C (30). However, these methods could not create a colloidal solution to fabricate the compact BSO perovskite film. Thus, the development of a mass-producible and completely dispersed precursor colloidal solution for producing BSO thin films is a challenging issue for obtaining efficient and photostable PSCs.

We first demonstrate a crystalline superoxide-molecular cluster (CSMC) colloidal solution containing well-dispersed CSMC NPs in 2-methoxyethanol (2ME) that was prepared by the reaction of BaCl<sub>2</sub>, SnCl<sub>2</sub>, La(NO<sub>3</sub>)<sub>3</sub>, and H<sub>2</sub>O<sub>2</sub> in an NH<sub>4</sub>OH aqueous solution at 50°C. We determined that the crystalline LBSO perovskite phase developed below 300°C from CSMC via an intermediate peroxy-complex by using extended x-ray absorption fine structure (EXAFS) analysis and density functional theory (DFT). The compact and uniform perovskite LBSO layer was successfully fabricated from the CSMC colloidal solution by spin-coating onto a fluorine-doped SnO<sub>2</sub> (FTO) substrate. To fabricate PSCs with the LBSO as an ETL, we used methylammonium lead iodide (MAPbI<sub>3</sub>) as a light harvester, because MAPbI<sub>3</sub>, which has a higher conduction band edge than formamidinium lead iodide (FAPbI<sub>3</sub>), is more suitable for the energy level of the LBSO electrode. The best-performing PSC exhibited a PCE of 21.2% (the highest value reported for MAPbI<sub>3</sub>-based PSCs) and a very high photostability below a 10% change for the PCE after 1000 hours of full-Sun illumination [including UV radiation, air mass (AM) 1.5G, 100 mW cm<sup>-2</sup>].

The crystalline phase of LBSO (used as an electrode in this study) is the same as that of pure BSO, as shown in fig. S1 (31), and we used undoped BSO as a model system to investigate the formation of LBSO at a low temperature. For the colloidal solution, Ba and Sn precursors were dissolved in a hydrogen peroxide (H<sub>2</sub>O<sub>2</sub>) aqueous solution (30% H<sub>2</sub>O<sub>2</sub>) at 50°C and room temperature (RT). A mass-producible white powder (>92% yield) was obtained by adjusting the pH from 1 to 10 by addition of NH<sub>4</sub>OH at 50°C, and the as-prepared powder was well dispersed in 2ME (fig. S2) (31). Figure 1A shows a representative scanning electron microscopy (SEM) image of the as-prepared powder synthesized at 50°C. The SEM image exhibits highly dispersed and defined NPs whose size distribution is shown in fig. S3 (31). The col-

loidal solution is highly transparent because individual discrete NPs (versus aggregates) form by a self-condensation reaction in the H<sub>2</sub>O<sub>2</sub>-assisted process. Figure 1B shows x-ray diffraction (XRD) patterns, measured in air, of the as-prepared and annealed powders. The spectrum for the as-prepared powder obtained via the CSMC route contains crystalline XRD peaks, whereas the conventional route (at RT) produces an amorphous powder (Fig. 1B).

The crystalline white powder was successfully converted into a pure perovskite BSO phase by annealing for 30 min at 200°C, which requires a much shorter time and lower temperature than a conventional route such as a solid-state reaction and sol-gel process for the pure BSO perovskite phase (32). By contrast, the amorphous powder produced at RT did not convert to the perovskite phase even at a much higher temperature (500°C). Thus, the initial crystalline phase in the as-prepared powder plays a key role in the formation of the BSO perovskite phase at 200°C. The XRD pattern of the as-prepared powder shown in Fig. 1B indicates that the initial crystalline phase is not an ideal cubic BSO perovskite phase. Infrared (IR) spectroscopic analysis was performed to identify the constituents in the as-prepared crystalline powders. Figure 1C shows Fourier transform (FT) infrared (IR) spectra of the as-prepared powders synthesized at 50°C and RT. The amorphous powder synthesized at RT shows stretching frequencies at 856 cm<sup>-1</sup> and 1400 to 1500 cm<sup>-1</sup>, which are assigned to  $\nu(O-O)$  and  $\delta(O-O-H)$  vibrations (33), respectively, revealing that the powder includes hydroperoxy (O-O-H) ligands. The hydroperoxy ligands were previously observed for amorphous or crystalline peroxy-precursors in H<sub>2</sub>O<sub>2</sub>-assisted methods (30, 33–35). The amorphous peroxy complexes exist as AMO<sub>2</sub>(O<sub>2</sub>)·3H<sub>2</sub>O (A is Ca, Sr, or Ba; M is Ti or Sn), which can be rewritten as A[M(OH)<sub>5</sub>(OOH)] (35). Therefore, these compounds are assumed to exist in the amorphous phase when prepared at RT. In addition, the crystalline structures consisting of alkaline metal cations and the hexahydroperoxostannate anion ([Sn(OOH)<sub>6</sub>]<sup>2-</sup>) have been reported through the substitution of the hydroxo ligands of the hydroxostannate precursor ([Sn(OH)<sub>6</sub>]<sup>2-</sup>) by a reaction with concentrated H<sub>2</sub>O<sub>2</sub> (33, 34). However, for the crystalline powder prepared at 50°C, the broad absorption related to the hydroperoxy ligand at 1400 to 1500 cm<sup>-1</sup> decreased and new IR absorption peaks at 1054 and 1098 cm<sup>-1</sup> are observed, which are ascribed to vibrations of the superoxo (O<sub>2</sub><sup>-</sup>) ligand with a shorter O-O bond length than the peroxy ligand (36). The powder is different from previously reported amorphous and crystalline peroxy-precursors for BSO perovskite (28, 30, 34, 35).

On the basis of controlled experiments examining the effects of temperature and H<sub>2</sub>O<sub>2</sub> concentration (fig. S4) (31), a schematic formation map for the superoxide precursor col-

loidal solution is shown in Fig. 1D. In the precipitates of  $\text{Sn}(\text{OOH})_x(\text{OH})_{4-x}$  formed from  $\text{H}_2\text{O}_2$  and  $\text{NH}_4\text{OH}$  mixture in aqueous solution, the value of  $x$  will increase with increasing amount of  $\text{H}_2\text{O}_2$  (33). The decomposition of  $\text{H}_2\text{O}_2$  is affected by various environmental conditions such as heat, catalysis, concentration of  $\text{H}_2\text{O}_2$ , and pH (37). As shown in Fig. 1D, the formation of superoxide ( $\text{SnO-O-Sn}$ ) will be more favorable at a higher  $x$  value and at a mild temperature below 90°C via the condensation reaction between  $-\text{OOH}$  ions. According to previous reports (37), the decomposition of  $\text{H}_2\text{O}_2$  was limited below 30°C at pH 10 to 11, whereas the increase in temperature from 30° to 40°C accelerated the decomposition rate of  $\text{H}_2\text{O}_2$  up to 3.3-fold at pH 10 to 11. Indeed, we observed that the crystalline superoxide complex appears at solution temperatures between 40° and 70°C (fig. S4A) (31), whereas reaction temperatures above 90°C decrease crystallinity (fig. S4A) (31). Furthermore, the crystalline phase is formed only at  $\text{H}_2\text{O}_2$  concentrations above 15% (fig. S4B) (31). Under these specific conditions (50°C and 30%), CSMC can be rapidly formed even within 10 min (fig. S4C) (31). An adequate temperature and high concentration of  $\text{H}_2\text{O}_2$  accelerate the formation of superoxide during the reaction that then forms the CSMC. The superoxo groups at surface of CSMC NPs tend to efficiently repel each other via surface charge, which lead to the stable colloidal solution. However, the CSMC phase formed at 90°C does not create colloidal solution because a sizable fraction of superoxide decomposes to form oxygen.

To elucidate the initial crystalline phase of CSMC and the phase-converting procedure from the initial phase to the BSO perovskite phase at low temperatures, we performed *in situ* EXAFS analysis for the initial crystalline powder in air as a function of temperature. Figure 2A shows the temperature-dependent radial distribution functions (RDFs) of Fourier-transformed (FT) Sn K-edge EXAFS spectra for the as-prepared CSMC powder. The initial powder showed a single strong peak at 1.58 Å, corresponding to the first oxygen shell. No meaningful peak intensity was observed for the higher radial space regions until heating to 150°C. The distinct singlet RDF feature means that the Sn-O bonds did not have long-range order in the initial crystalline powder, reflecting the existence of single molecular clusters of  $\text{Sn}-\text{O}_x$ . However, a small FT peak at 4.17 Å developed at 160°C and gradually increased until 180°C. Considering the uncorrected phase shift ( $\mathbf{r}_{\text{eff}}$  is higher than ~0.4 Å), the FT peak is not attributed to the BSO perovskite phase but might result from  $\text{Sn}-\text{O}_2^{2-}-\text{Sn}$  in the intermediate phase that includes the peroxy anion ( $\text{O}_2^{2-}$ ) because the initial crystalline powder includes superoxo ligands. After the complete disappearance of the FT peak at 190°C, new doublet FT peaks evolved at 3.31 and 3.84 Å at 200°C. The FT peaks correspond to the characteristic overall RDF feature of Sn-Ba and corner-

shared Sn-(O)-Sn distributions for the BSO perovskite crystal structure, respectively, revealing that the as-prepared white powder was effectively converted to the pure perovskite phase during the *in situ* experiment at 200°C. Thus, the formation of a superoxide molecular cluster with a perovskite frame can facilitate the synthesis of well-dispersed perovskite BSO NPs, even below 500°C.

On the basis of the XRD, IR, and temperature-dependent RDF results, we performed a first-principles calculation using DFT to elucidate the origin of the phase evolution to BSO perovskite below 200°C (crystal structures are shown in Fig. 2B). The CSMC has structural deformations from cubic symmetry because the octahedral consisting of Sn and six  $\text{O}_2^-$  molecules maintain their local geometries but have randomly distributed orientations. This long-range-ordered single cluster consisting of  $\text{Ba}^{2+}$  cations and the hexasuperoxostannate anion,  $[\text{Sn}(\text{O}-\text{O})_6]^{2-}$ , in the as-prepared powder initially formed cross-linked  $\text{Sn}-[\text{O}-\text{O}]-\text{Sn}$  octahedra with the removal of  $\text{O}_2$  during heating; the higher temperature promotes long-range-ordered development of corner-shared Sn-(O)-Sn octahedra by way of  $\text{O}_2$  removal, finally revealing the pure cubic BSO perovskite structure. We hypothesized that the formation of the long-range-ordered single cluster as a precursor requires lower energy and presents a faster pathway to the thermodynamically stable cubic perovskite BSO phase, as compared to starting from the amorphous phase.

The phase evolution from CSMCs to pure BSO perovskite makes it possible to fabricate a LBSO film as an n-type layer for PSCs on a transparent conductive oxide (TCO) glass substrate below 500°C by coating with the CSMC colloidal solution. Figure 2C shows a SEM image of an LBSO film deposited by a spin-coating method using the CSMC colloidal solution with sequential annealing. The film is crack-free and provides uniform, continuous coverage of the substrate with densely packed LBSO NPs. Moreover, the surface roughness of the film is very low (~5 nm root-mean-square roughness) as measured by atomic force microscopy (AFM). The XRD spectra for as-coated and annealed LBSO films are shown in fig. S5 (31). Analyses confirmed that La cations were successfully doped into BSO perovskite to form the final LBSO film for use as an ETL in PSCs (fig. S6) (31).

Figure 3A shows a cross-sectional SEM image of the PSC fabricated by a solvent-engineering process (38) with  $\text{MAPbI}_3$  as a halide perovskite material and PTAA as an HTL. The PSC consisted of uniform layers of a LBSO perovskite oxide layer (~120 nm in thickness) and a uniformly deposited upper layer (~440 nm in thickness) of  $\text{MAPbI}_3$ . In Fig. 3B, photocurrent density-voltage ( $J-V$ ) characteristics of the PSC fabricated with LBSO as an ETL are presented and compared with those of a control device by using  $\text{mp-TiO}_2$ , which is a typical ETL for fabricating highly efficient PSCs.

As shown in the *J-V* curves, the LBSO cell exhibited an open-circuit voltage ( $V_{oc}$ ) of 1.12 V, a short-circuit current density ( $J_{sc}$ ) of 23.4 mA/cm<sup>2</sup>, and a fill factor ( $FF$ ) of 81.3%, giving an overall PCE of 21.3%, whereas the control device showed an overall PCE of 19.6% with a  $V_{oc}$  of 1.07 V, a  $J_{sc}$  of 23.3 mA/cm<sup>2</sup>, and a  $FF$  of 78.6%. The superior performance of the LBSO PSC is mainly attributed to a higher  $V_{oc}$  and  $FF$ , which are associated with beneficial effects such as a higher conduction band minimum and electron density of LBSO, and reduced carrier recombination compared to mp-TiO<sub>2</sub>. Because the PSCs using LBSO as the ETL exhibited a large hysteresis in their *J-V* curves with reverse and forward sweeps (fig. S7) (31), the stabilized PCEs were estimated to determine the real power output of the device by measuring the steady-state photocurrent with an applied voltage at the maximum power point under simulated solar illumination (100 mW cm<sup>-2</sup>, AM 1.5G). The LBSO PSC showed a stabilized power output of 21.2% near the maximum power point (0.96 V), which closely matched the values extracted from the *J-V* curve with a reverse sweep (Fig. 3B, inset), whereas the TiO<sub>2</sub>-based device showed a stabilized PCE of 19.7%. The reverse-sweep *J-V* curve for the LBSO PSC is notable, although the underestimated forward-sweep *J-V* curve requires further study. Figure S8 shows the time-correlated single-photon counting (TCSPC) results for perovskite samples on different substrates (glass, TiO<sub>2</sub>, and LBSO) to investigate the photoinduced carrier kinetics inside the perovskite layer (31). The LBSO sample provides faster emission quenching than the TiO<sub>2</sub> sample, which seems to be caused by a more efficient electron injection. In addition to the efficient electron injection, the high electron density created by La-doping in BSO might cause a large built-in potential at the junction between perovskite and the n-type layer (12), which seems to result in a superior PV performance. That the high electron density contributes to the improvement of  $V_{oc}$  and  $FF$  becomes clearer in comparison with the undoped BSO (fig. S9) (31), because optical properties of 5 mol % La-doped BSO are only changed by a small amount (39), indicating a widely constant position of the conduction band edge. Figure 3C shows the external quantum efficiency (EQE) spectrum and integrated  $J_{sc}$  values for one of the LBSO PSCs. The high  $J_{sc}$  value is attributed to a very broad EQE plateau above 85% between 400 and 750 nm. The  $J_{sc}$  value obtained by integrating the EQE spectrum is 23.2 mA cm<sup>-2</sup>, which agrees with the measured value of 23.4 mA cm<sup>-2</sup> in Fig. 3B. Figure 3D presents the histogram for PCEs extracted from the stabilized PCEs at the maximum power point. High-efficiency solar cells with average stabilized PCE of 20.3% (maximum and minimum values of 21.2 and 19.7%, respectively) could be achieved with a high degree of reproducibility by using the LBSO electron collection layer.

One of the most important requirements for PSCs is pho-

tostability under light illumination, including UV. The marked UV-induced degradation in PCEs for TiO<sub>2</sub>-based PSCs presents a serious problem (14, 15, 18) for their practical use under natural sunlight. So far, PSCs claiming photostability have been tested with white light-emitting diode or UV-filtered solar simulators (40, 41). We conducted a light-soaking experiment by monitoring the *J-V* characteristics under AM 1.5G illumination with a xenon or metal-halide lamp, including UV radiation to estimate the photostability under 1-sun illumination for the LBSO- and TiO<sub>2</sub>-based PSCs. Figure 4A shows the monitored PCEs of the unencapsulated FTO/LBSO/MAPbI<sub>3</sub>/PTAA/Au and FTO/TiO<sub>2</sub>/MAPbI<sub>3</sub>/PTAA/Au devices in a nitrogen-filled chamber with a constant device temperature of 25°C and constant AM 1.5G illumination with a xenon lamp. The LBSO cell showed a greater resistance against photodegradation than the TiO<sub>2</sub> cell; the latter showed an abrupt decrease in PCE upon initial illumination.

However, a cell architecture that includes organic hole-transport materials (HTMs), such as PTAA or spiro-OMeTAD, is inappropriate for estimating the influence of n-type materials on the photostability for long-term measurements (~1000 hours) because organic HTMs can degrade the PV performance by morphological deformation, metal diffusion, movable additives, and so forth. To exclude the influence of organic HTMs on the photostability test, we fabricated a two-sided glass-encapsulated architecture using an inorganic p-type NiO layer instead of the organic HTM layer, which is glass/FTO/n-type oxide/MAPbI<sub>3</sub>/NiO/FTO/glass, by lamination of two half cells (glass/FTO/n-type oxide/MAPbI<sub>3</sub> and MAPbI<sub>3</sub>/NiO/FTO/glass). The fabrication procedure and initial photovoltaic performance for the laminate cell are described in fig. S10 (31). PCEs in encapsulated BSO and TiO<sub>2</sub> cells were monitored by measuring *J-V* curves in air under AM 1.5G illumination with a metal-halide lamp, including UV radiation; a spectrum is presented in fig. S11 (31). The LBSO cell retained 93.3% of its initial performance after 1000 hours, whereas the TiO<sub>2</sub> cell completely degraded within 500 hours (Fig. 4B). The development of the n-type BSO perovskite moves us a step closer to PSC commercialization by eliminating the requirement of the additional UV filter for previous TiO<sub>2</sub> PSCs.

## REFERENCES AND NOTES

1. M. M. Lee, J. Teuscher, T. Miyasaka, T. N. Murakami, H. J. Snaith, Efficient hybrid solar cells based on meso-superstructured organometal halide perovskites. *Science* **338**, 643–647 (2012). doi:10.1126/science.1228604 Medline
2. H.-S. Kim, C.-R. Lee, J.-H. Im, K.-B. Lee, T. Moehl, A. Marchioro, S.-J. Moon, R. Humphry-Baker, J.-H. Yum, J. E. Moser, M. Grätzel, N.-G. Park, Lead iodide perovskite sensitized all-solid-state submicron thin film mesoscopic solar cell with efficiency exceeding 9%. *Sci. Rep.* **2**, 591 (2012). doi:10.1038/srep00591 Medline
3. A. Kojima, K. Teshima, Y. Shirai, T. Miyasaka, Organometal halide perovskites as visible-light sensitizers for photovoltaic cells. *J. Am. Chem. Soc.* **131**, 6050–6051

- (2009). doi:10.1021/ja809598r Medline
4. M. Saliba, T. Matsui, K. Domanski, J.-Y. Seo, A. Ummadisingu, S. M. Zakeeruddin, J.-P. Correa-Baena, W. R. Tress, A. Abate, A. Hagfeldt, M. Grätzel, Incorporation of rubidium cations into perovskite solar cells improves photovoltaic performance. *Science* **354**, 206–209 (2016). doi:10.1126/science.aah5557 Medline
  5. W. S. Yang, J. H. Noh, N. J. Jeon, Y. C. Kim, S. Ryu, J. Seo, S. I. Seok, SOLAR CELLS. High-performance photovoltaic perovskite layers fabricated through intramolecular exchange. *Science* **348**, 1234–1237 (2015). doi:10.1126/science.aaa9272 Medline
  6. J. H. Heo, S. H. Im, J. H. Noh, T. N. Mandal, C.-S. Lim, J. A. Chang, Y. H. Lee, H. Kim, A. Sarkar, M. K. Nazeeruddin, M. Grätzel, S. I. Seok, Efficient inorganic-organic hybrid heterojunction solar cells containing perovskite compound and polymeric hole conductors. *Nat. Photonics* **7**, 486–491 (2013). doi:10.1038/nphoton.2013.80
  7. M. Liu, M. B. Johnston, H. J. Snaith, Efficient planar heterojunction perovskite solar cells by vapour deposition. *Nature* **501**, 395–398 (2013). doi:10.1038/nature12509 Medline
  8. O. Malinkiewicz, A. Yella, Y. H. Lee, G. M. Espallargas, M. Graetzel, M. K. Nazeeruddin, H. J. Bolink, Perovskite solar cells employing organic charge-transport layers. *Nat. Photonics* **8**, 128–132 (2014). doi:10.1038/nphoton.2013.341
  9. D.-Y. Son, J.-H. Im, H.-S. Kim, N.-G. Park, 11% efficient perovskite solar cell based on ZnO nanorods: An effective charge collection system. *J. Phys. Chem. C* **118**, 16567–16573 (2014). doi:10.1021/jp412407j
  10. J. P. Correa-Baena, L. Steier, W. Tress, M. Saliba, S. Neutzner, T. Matsui, F. Giordano, T. J. Jacobsson, A. R. Srimath Kandada, S. M. Zakeeruddin, Highly efficient planar perovskite solar cells through band alignment engineering. *Energy Environ. Sci.* **8**, 2928–2934 (2015). doi:10.1039/C5FE02608C
  11. S. S. Shin, W. S. Yang, J. H. Noh, J. H. Suk, N. J. Jeon, J. H. Park, J. S. Kim, W. M. Seong, S. I. Seok, High-performance flexible perovskite solar cells exploiting Zn<sub>2</sub>SnO<sub>4</sub> prepared in solution below 100 °C. *Nat. Commun.* **6**, 7410 (2015). doi:10.1038/ncomms8410 Medline
  12. S. S. Shin, W. S. Yang, E. J. Yeom, S. J. Lee, N. J. Jeon, Y.-C. Joo, I. J. Park, J. H. Noh, S. I. Seok, Tailoring of electron-collecting oxide nanoparticulate layer for flexible perovskite solar cells. *J. Phys. Chem. Lett.* **7**, 1845–1851 (2016). doi:10.1021/acs.jpclett.6b00295 Medline
  13. G. Niu, X. Guo, L. Wang, Review of recent progress in chemical stability of perovskite solar cells. *J. Mater. Chem. A Mater. Energy Sustain.* **3**, 8970–8980 (2015). doi:10.1039/C4TA04994B
  14. W. Li, W. Zhang, S. Van Reenen, R. J. Sutton, J. Fan, A. A. Haghhighirad, M. B. Johnston, L. Wang, H. J. Snaith, Enhanced UV-light stability of planar heterojunction perovskite solar cells with caesium bromide interface modification. *Energy Environ. Sci.* **9**, 490–498 (2016). doi:10.1039/C5FE03522H
  15. T. Leijtens, G. E. Eperon, S. Pathak, A. Abate, M. M. Lee, H. J. Snaith, Overcoming ultraviolet light instability of sensitized TiO<sub>2</sub> with meso-superstructured organometal tri-halide perovskite solar cells. *Nat. Commun.* **4**, 2885 (2013). doi:10.1038/ncomms3885 Medline
  16. S. Guarnera, A. Abate, W. Zhang, J. M. Foster, G. Richardson, A. Petrozza, H. J. Snaith, Improving the long-term stability of perovskite solar cells with a porous Al<sub>2</sub>O<sub>3</sub> buffer layer. *J. Phys. Chem. Lett.* **6**, 432–437 (2015). doi:10.1021/jz502703p Medline
  17. H. Tsai, W. Nie, J.-C. Blancon, C. C. Stoumpos, R. Asadpour, B. Harutyunyan, A. J. Neukirch, R. Verduzco, J. J. Crochet, S. Tretiak, L. Pedesseau, J. Even, M. A. Alam, G. Gupta, J. Lou, P. M. Ajayan, M. J. Bedzyk, M. G. Kanatzidis, A. D. Mohite, High-efficiency two-dimensional Ruddlesden-Popper perovskite solar cells. *Nature* **536**, 312–316 (2016). doi:10.1038/nature18306 Medline
  18. F. Bella, G. Griffini, J.-P. Correa-Baena, G. Saracco, M. Grätzel, A. Hagfeldt, S. Turri, C. Gerbaldi, Improving efficiency and stability of perovskite solar cells with photocurable fluoropolymers. *Science* **354**, 203–206 (2016). doi:10.1126/science.aah4046 Medline
  19. S. Ito, S. Tanaka, K. Manabe, H. Nishino, Effects of surface blocking layer of Sb<sub>2</sub>S<sub>3</sub> on nanocrystalline TiO<sub>2</sub> for CH<sub>3</sub>NH<sub>3</sub>PbI<sub>3</sub> perovskite solar cells. *J. Phys. Chem. C* **118**, 16995–17000 (2014). doi:10.1021/jp500449z
  20. S. K. Pathak, A. Abate, P. Ruckdeschel, B. Roose, K. C. Gödel, Y. Vaynzof, A. Santhala, S. I. Watanabe, D. J. Hollman, N. Noel, A. Sepe, U. Wiesner, R. Friend, H. J. Snaith, U. Steiner, Performance and stability enhancement of dye-sensitized and perovskite solar cells by Al doping of TiO<sub>2</sub>. *Adv. Funct. Mater.* **24**, 6046–6055 (2014). doi:10.1002/adfm.201401658
  21. D. O. Scanlon, Defect engineering of BaSnO<sub>3</sub> for high-performance transparent conducting oxide applications. *Phys. Rev. B* **87**, 161201 (2013). doi:10.1103/PhysRevB.87.161201
  22. Y. M. Kim, C. Park, U. Kim, C. Ju, K. Char, High-mobility BaSnO<sub>3</sub> thin-film transistor with HfO<sub>2</sub> gate insulator. *Appl. Phys. Express* **9**, 011201 (2015). doi:10.7567/APFX.9.011201
  23. J. Cerdà, J. Arbiol, G. Dezanneau, R. Diaz, J. Morante, Perovskite-type BaSnO<sub>3</sub> powders for high temperature gas sensor applications. *Sens. Actuators B Chem.* **84**, 21–25 (2002). doi:10.1016/S0925-4005(02)00005-9
  24. H. J. Kim, U. Kim, H. M. Kim, T. H. Kim, H. S. Mun, B.-G. Jeon, K. T. Hong, W.-J. Lee, C. Ju, K. H. Kim, K. Char, High mobility in a stable transparent perovskite oxide. *Appl. Phys. Express* **5**, 061102 (2012). doi:10.1143/APEX.5.061102
  25. W. Zhang, J. Tang, J. Ye, Photoluminescence and photocatalytic properties of SrSnO<sub>3</sub> perovskite. *Chem. Phys. Lett.* **418**, 174–178 (2006). doi:10.1016/j.cplett.2005.10.122
  26. W. Wang, S. Liang, K. Ding, J. Bi, J. C. Yu, P. K. Wong, L. Wu, Microwave hydrothermal synthesis of MSnO<sub>3</sub> (M<sup>2+</sup>= Ca<sup>2+</sup>, Sr<sup>2+</sup>, Ba<sup>2+</sup>): Effect of M<sup>2+</sup> on crystal structure and photocatalytic properties. *J. Mater. Sci.* **49**, 1893–1902 (2014). doi:10.1007/s10853-013-7880-x
  27. P. Wadekar, J. Alaria, M. O'Sullivan, N. Flack, T. Manning, L. Phillips, K. Durose, O. Lozano, S. Lucas, J. Claridge, M. J. Rosseinsky, Improved electrical mobility in highly epitaxial La: BaSnO<sub>3</sub> films on SmScO<sub>3</sub> (110) substrates. *Appl. Phys. Lett.* **105**, 052104 (2014). doi:10.1063/1.4891816
  28. G. Pfaff, Wet chemical synthesis of BaSnO<sub>3</sub> and Ba<sub>2</sub>SnO<sub>4</sub> powders. *J. Eur. Ceram. Soc.* **12**, 159–164 (1993). doi:10.1016/0955-2219(93)90137-G
  29. S. S. Shin, J. S. Kim, J. H. Suk, K. D. Lee, D. W. Kim, J. H. Park, I. S. Cho, K. S. Hong, J. Y. Kim, Improved quantum efficiency of highly efficient perovskite BaSnO<sub>3</sub>-based dye-sensitized solar cells. *ACS Nano* **7**, 1027–1035 (2013). doi:10.1021/nn305341x Medline
  30. C. Huang, X. Wang, Q. Shi, X. Liu, Y. Zhang, F. Huang, T. Zhang, A facile peroxo-precursor synthesis method and structure evolution of large specific surface area mesoporous BaSnO<sub>3</sub>. *Inorg. Chem.* **54**, 4002–4010 (2015). doi:10.1021/acs.inorgchem.5b00269 Medline
  31. See supplementary materials.
  32. J. Cerdà, J. Arbiol, R. Diaz, G. Dezanneau, J. Morante, Synthesis of perovskite-type BaSnO<sub>3</sub> particles obtained by a new simple wet chemical route based on a sol-gel process. *Mater. Lett.* **56**, 131–136 (2002). doi:10.1016/S0167-577X(02)00428-7
  33. S. Sladkevich, V. Gutkin, O. Lev, E. A. Legurova, D. F. Khabibulin, M. A. Fedotov, V. Uvarov, T. A. Tripol'skaya, P. V. Prikhodchenko, Hydrogen peroxide induced formation of peroxystannane nanoparticles. *J. Sol-Gel Sci. Technol.* **50**, 229–240 (2009). doi:10.1007/s10971-008-1800-6
  34. A. V. Churakov, S. Sladkevich, O. Lev, T. A. Tripol'skaya, P. V. Prikhodchenko, Cesium hydroperoxostannate: First complete structural characterization of a homoleptic hydroperoxocomplex. *Inorg. Chem.* **49**, 4762–4764 (2010). doi:10.1021/ic100554u Medline
  35. G. Pfaff, V. Hildenbrand, H. Fuess, Spectroscopic study of amorphous precursors for alkaline-earth titanates and stannates, *J. Mater. Sci. Lett.* **17**, 1983–1985 (1998). doi:10.1023/A:1006652405086
  36. Y. Zhao, B.-T. Teng, X.-D. Wen, Y. Zhao, Q.-P. Chen, L.-H. Zhao, M.-F. Luo, Superoxide and peroxide species on CeO<sub>2</sub> (111), and their oxidation roles. *J. Phys. Chem. C* **116**, 15986–15991 (2012). doi:10.1021/jp3016326
  37. E. Yazici, H. Deveci, Factors affecting decomposition of hydrogen peroxide, in *Proceedings of the XII International Mineral Processing Symposium (IMPS)*, 6 to 8 October 2010, Cappadocia- Nevşehir, Turkey, O. Y. Gulsoy, S. L. Ergun, N. M. Can, I. B. Celik, Eds. (Hacettepe University, Department of Mining Engineering, 2010), pp. 609–616.
  38. N. J. Jeon, J. H. Noh, Y. C. Kim, W. S. Yang, S. Ryu, S. I. Seok, Solvent engineering for high-performance inorganic-organic hybrid perovskite solar cells. *Nat. Mater.* **13**, 897–903 (2014). doi:10.1038/nmat4014 Medline
  39. K. K. James, P. S. Krishnaprasad, K. Hasna, M. K. Jayaraj, Structural and optical

- properties of La-doped BaSnO<sub>3</sub> thin films grown by PLD. *J. Phys. Chem. Solids* **76**, 64–69 (2015). doi:10.1016/j.jpcs.2014.07.024
40. M. Saliba, T. Matsui, J.-Y. Seo, K. Dornanski, J.-P. Correa-Baena, M. K. Nazeeruddin, S. M. Zakeeruddin, W. Tress, A. Abate, A. Hagfeldt, M. Grätzel, Cesium-containing triple cation perovskite solar cells: Improved stability, reproducibility and high efficiency. *Energy Environ. Sci.* **9**, 1989–1997 (2016). doi:10.1039/C5EE03874J Medline
41. W. Chen, Y. Wu, Y. Yue, J. Liu, W. Zhang, X. Yang, H. Chen, E. Bi, I. Ashraful, M. Grätzel, L. Han, Efficient and stable large-area perovskite solar cells with inorganic charge extraction layers. *Science* **350**, 944–948 (2015). doi:10.1126/science.aad1015 Medline
42. X. Luo, Y. S. Oh, A. Sirenko, P. Gao, T. Tyson, K. Char, S.-W. Cheong, High carrier mobility in transparent Ba<sub>1-x</sub>La<sub>x</sub>SnO<sub>3</sub> crystals with a wide band gap. *Appl. Phys. Lett.* **100**, 172112 (2012). doi:10.1063/1.4709415
43. Z. Lebens-Higgins, D. O. Scanlon, H. Paik, S. Sallis, Y. Nie, M. Uchida, N. F. Quackenbush, M. J. Wahila, G. E. Sterbinsky, D. A. Arena, J. C. Woicik, D. G. Schlom, L. F. J. Piper, Direct observation of electrostatically driven band gap renormalization in a degenerate perovskite transparent conducting oxide. *Phys. Rev. Lett.* **116**, 027602 (2016). doi:10.1103/PhysRevLett.116.027602 Medline
44. C. Shan, T. Huang, J. Zhang, M. Han, Y. Li, Z. Hu, J. Chu, Optical and electrical properties of sol-gel derived Ba<sub>1-x</sub>La<sub>x</sub>SnO<sub>3</sub> transparent conducting films for potential optoelectronic applications. *J. Phys. Chem. C* **118**, 6994–7001 (2014). doi:10.1021/jp500100a
45. B. Luo, J. Zhang, J. Wang, P. Ran, Structural, electrical and optical properties of lanthanum-doped barium stannate. *Ceram. Int.* **41**, 2668–2672 (2015). doi:10.1016/j.ceramint.2014.10.080
46. A. Nelson, J. Adams, K. Schaffers, Photoemission investigation of the electronic structure of lanthanum–calcium oxaborate. *J. Appl. Phys.* **94**, 7493–7495 (2003). doi:10.1063/1.1627955

## ACKNOWLEDGMENTS

This work was supported by Global Frontier R&D Program for Multiscale Energy System (NRF-2011-0031565, NRF-2016M3A6A7945503), Climate Change Program (NRF-2015M1A2A2056542), and Wearable Platform Materials Technology Center (WMC-no. 2016R1A5A1009926) through the National Research Foundation of Korea (NRF) funded by the Ministry of Science, ICT, and Future Planning. This work was also financially supported by the KIST-UNIST partnership program (I.160097.01/2.160482.01). All data are presented in the main text and supplementary materials. S.S.S., J.H.N., J.S., and S.I.S. are inventors on a patent application (KR 10-2016-0040923) submitted by the Korea Research Institute of Chemical Technology and Ulsan National Institute of Science and Technology that covers the preparation of Ba(La)SnO<sub>3</sub> particles and film at low temperature. Dr. Shin and Dr. Noh dedicate this paper to the memory of Prof. Kug Sun Hong, who passed away on 14 March 2014.

## SUPPLEMENTARY MATERIALS

[www.sciencemag.org/cgi/content/full/science.aam6620/DC1](http://www.sciencemag.org/cgi/content/full/science.aam6620/DC1)

Materials and Methods

Figs. S1 to S11

References (42–46)

23 December 2016; accepted 3 March 2017

Published online 30 March 2017

10.1126/science.aam6620

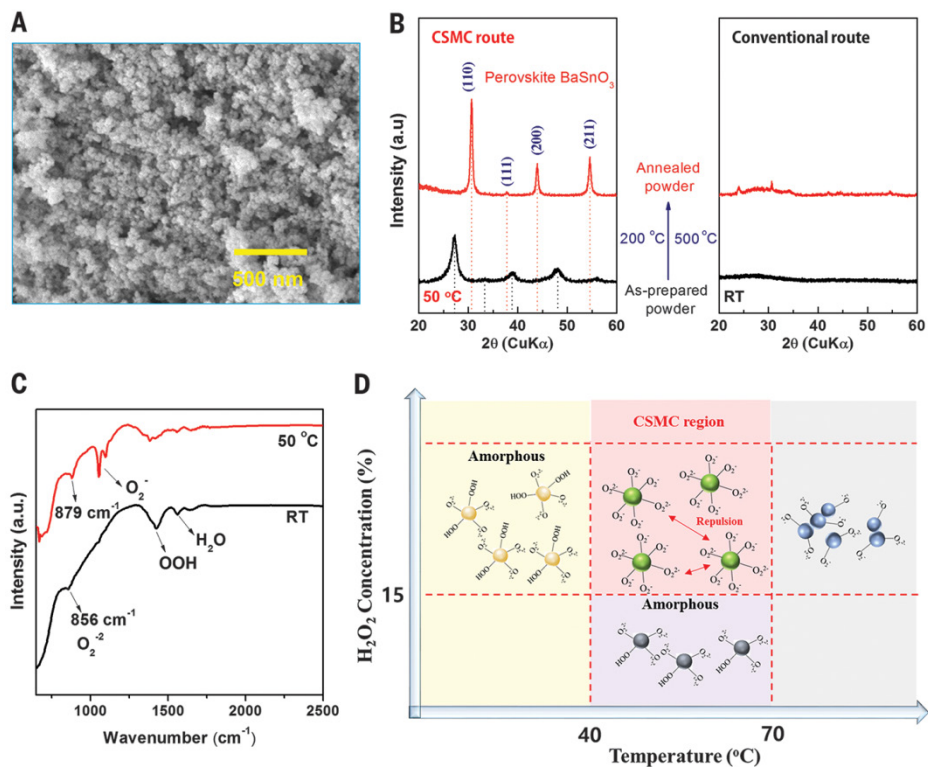


**Fig. 1. Synthesis of CSMC and BSO.** (A) SEM image of the as-prepared BSO powder synthesized at 50°C. (B) XRD spectra of the as-prepared powder synthesized at 50°C and annealed powder at 200°C for 30 min (left), and the as-prepared powder synthesized at room temperature and annealed at 500°C for 1 hour via the conventional route (right). (C) FT-IR spectra of the as-prepared BSO powder synthesized at room temperature and 50°C. (D) Schematic illustration of the formation map for the superoxide precursor colloidal solution.

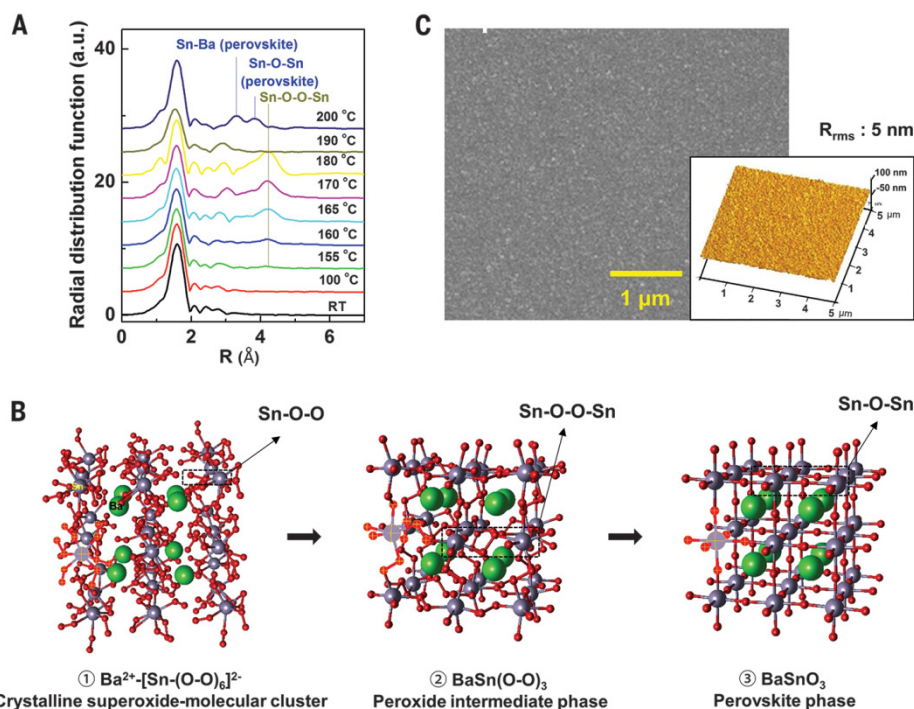


**Fig. 2. Formation process and DFT simulation.** (A) In situ EXAFS spectra (Sn K-edge) for the as-prepared powder (nonannealed powder) synthesized at 50°C with a heating rate of 0.5°C min<sup>-1</sup>. (B) Proposed crystal structure of the phase evolution in the CSMC route: (1) crystalline superoxide-molecular cluster consisting of Ba, Sn, and O<sub>2</sub><sup>2-</sup>; (2) peroxide intermediate phase, including the peroxy anion (O<sub>2</sub><sup>2-</sup>); and (3) BaSnO<sub>3</sub> perovskite phase (green, gray, and red spheres indicate Ba, Sn, and O ions, respectively). (C) SEM and 3D topographical AFM images of film deposited on FTO by spin-coating with the prepared LBSO colloidal solution.

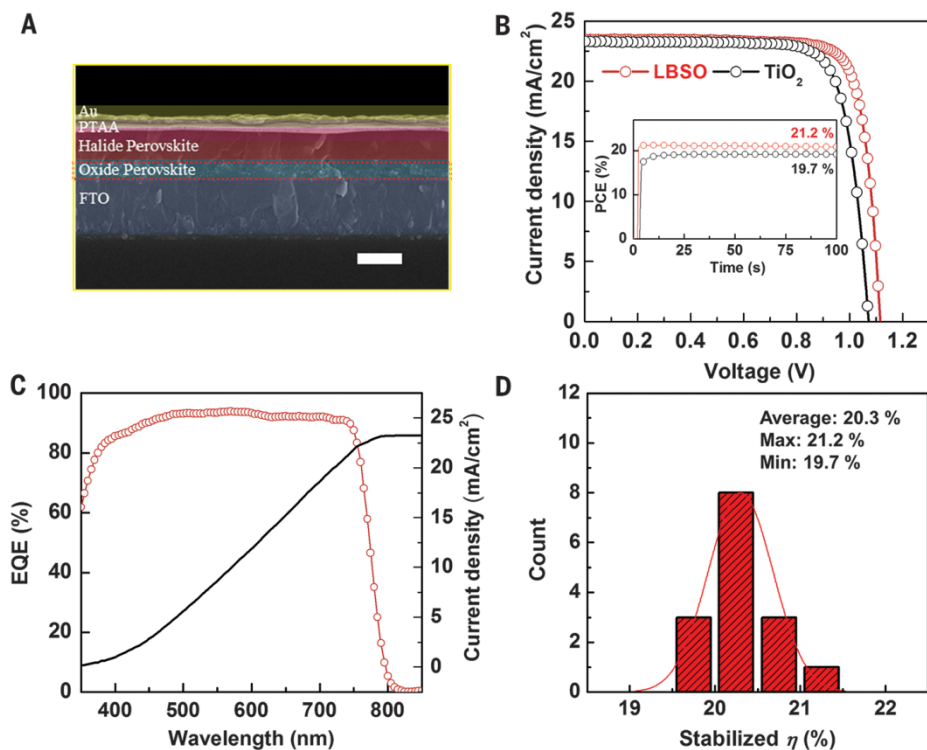


**Fig. 3. Photovoltaic performance of PSCs** (A) Cross-sectional SEM image of LBSO-based PSCs (scale bar, 500 nm). (B) J-V curves, and (inset) stabilized PCEs at a maximum power point (LBSO: 0.96 V; TiO<sub>2</sub>: 0.91V) for the best-performing LBSO- and TiO<sub>2</sub>-based PSC. (C) EQE spectrum and  $J_{sc}$  integrated from the EQE spectrum of the best-performing LBSO-based PSC. (D) Histograms of PCEs extracted from a photocurrent density stabilized at the maximum power point during 100 s for the LBSO-based PSCs.

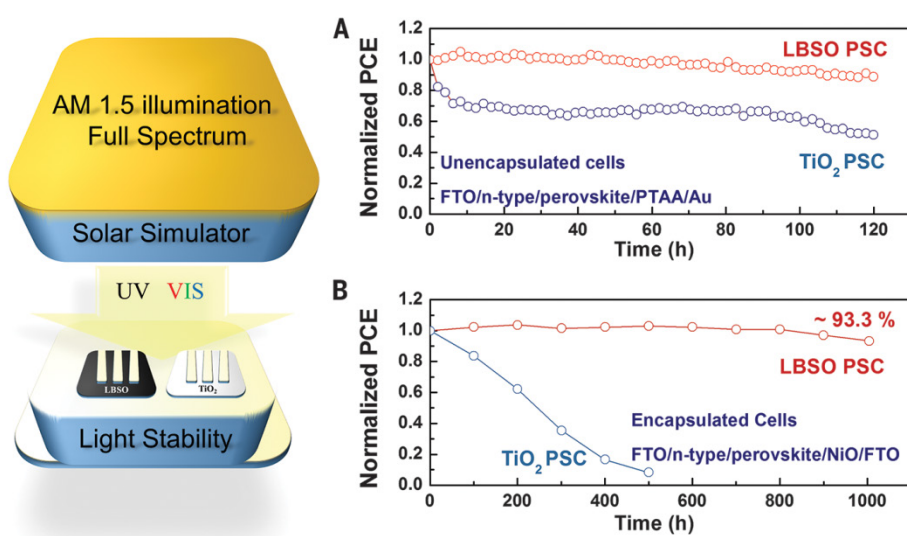


**Fig. 4. Photostability test of PSCs.** (A) Photostability tests under constant AM 1.5G illumination with a xenon lamp, including UV radiation for two unencapsulated devices of FTO/LBSO/MAPbI<sub>3</sub>/PTAA/Au and FTO/TiO<sub>2</sub>/MAPbI<sub>3</sub>/PTAA/Au. (B) Long-term photostability test under constant AM 1.5G illumination with a metal-halide lamp, including UV radiation for two encapsulated devices of FTO/LBSO/MAPbI<sub>3</sub>/NiO/FTO and FTO/TiO<sub>2</sub>/MAPbI<sub>3</sub>/NiO/FTO.



**Colloidally prepared La-doped BaSnO<sub>3</sub> electrodes for efficient, photostable perovskite solar cells**

Seong Sik Shin, Eun Joo Yeom, Woon Seok Yang, Seyoon Hur, Min Gyu Kim, Jino Im, Jangwon Seo, Jun Hong Noh and Sang Il Seok  
(March 30, 2017)

published online March 30, 2017

Editor's Summary

---

This copy is for your personal, non-commercial use only.

---

**Article Tools**

Visit the online version of this article to access the personalization and article tools:

<http://science.sciencemag.org/content/early/2017/03/29/science.aam6620>

**Permissions**

Obtain information about reproducing this article:

<http://www.sciencemag.org/about/permissions.dtl>

*Science* (print ISSN 0036-8075; online ISSN 1095-9203) is published weekly, except the last week in December, by the American Association for the Advancement of Science, 1200 New York Avenue NW, Washington, DC 20005. Copyright 2016 by the American Association for the Advancement of Science; all rights reserved. The title *Science* is a registered trademark of AAAS.